An analytical approach of design for recycling of laminate structures by the use of magnetic pulse disassembling

Benoit Lagain, Thomas Heuzé, Guillaume Racineux, Michel Arrigoni

An analytical approach of design for recycling of laminate structures by the use of magnetic pulse disassembling

Benoit Lagain[a,*], Thomas Heuzé[a], Guillaume Racineux[a], Michel Arrigoni[b]

[a] *Research Institute in Civil and Mechanical Engineering (GeM, UMR 6183 CNRS) Ecole Centrale de Nantes, 1 rue de la Noë, F-44321 Nantes, France*
[b] *ENSTA Bretagne, Institut de recherche Dupuy de Lôme (IRDL), UMR CNRS 6027, 29806 Brest, France*

Abstract

Composite materials in association with metal sheets or ceramic coatings have found a variety of applications, especially as load-bearing components in composite structures. Their disassembly for recycling or maintenance has therefore become more complex. The magnetic pulse technique, usually dedicated to dynamic forming and welding processes, can be used to separate composite materials of a laminate structure of their recyclable adjacent materials. This technology profits from Lorentz forces appearing in electrically conductive materials placed in the vicinity of conductors in which high-intensity electrical discharges are performed. These body forces act locally during the fast energy discharge, from which a stress wave propagates in the structure. The propagation of this stress wave can be used to generate interfacial tensile stress in laminate structures or assemblies. Especially, this technique can be used for evaluating the dynamic bond strength of an interface. This works aims at determining the required conditions for disassembling a laminate structure using a magnetic pulse imposed on one side of the assembly, without significantly damaging the debonded layers. Ideally, the generated interfacial tensile stress should be greater than the interfacial bond strength. In this paper, a one-dimensional analytical analysis is performed in linear elastodynamics on a tri-layered laminate structure, infinite in transverse directions, based on the method of characteristics. An optimisation problem is defined, maximising the interfacial stress between the first two layers, whose solution requires to study various configurations of the assembly involving different sets of characteristics in the laminate, associated with different areas of the domain of feasability spanned by the unknown vector. Some assumptions and introduced simplifications of the optimisation problem allows to follow a simple two-stage solution procedure, first with respect to the thickness of the first layer for a given stress pulse, then with respect to material impedances of all layers. Several configurations of the assembly are shown to create a sufficiently large interfacial tensile stress to reach the crack initiation and propagation, and a maximum tensile interface stress of twice the maximum applied pressure is obtained in the asymptotic limit.

Keywords: Magnetic pulse disassembly, Linear elastodynamics, Laminate structures, One-dimensional analytical solution, Optimisation problem

*Corresponding author
Email address: benoit.lagain@ec-nantes.fr (Benoit Lagain)

Postprint

Table of symbols

T	Appearance moment of the interface tensile stress
d_i	Width of the layer i
c_i	Longitudinal elastic sound speed of the material of layer i
Z_i	Acoustic wave impedance of the material of layer i
τ	Duration of the input pulse
P_{max}	Input pulse amplitude
$\sigma_{interface}$	Tensile stress at the interface at time $t = T$.
A_iB_j	Geometrical configuration where the wave does i round trip in the layer A and j in layer B before $t = T$.

Table 1: Symbols used in the article

1. Introduction

Material assemblies are more and more utilised in the design of load-bearing composite structures of high added value technologies [1, 9]. This kind of assemblies can associate light weight efficiency with durability, two performances required for a sustainable design. However, on the one hand, assembling different materials such as composite materials, ceramics and metals, durably and in a sustained production pace still remains a challenge for the industry. On the other hand, the assembly efficiency must be proved by suitable tests and controls. At last, recyclability and maintainability of manufactured goods has become of a major content for the future of our society.

With the idea of measuring the adhesion strength of an assembly method, various tests have been developed last decades [7, 26, 27]. The purpose of these tests are mostly to ensure the strength of the interface between two layers by creating acoustic waves in it [38, 25, 32, 33, 11] which will create tensile stress inside the tested structure. Several technologies can be used like the ARCAN test [8, 10, 31]. However, the ARCAN method does not allow the study of the dynamic behaviour of interfacial adhesion. In addition, it is essentially devoted to adhesively bonded assemblies. Other technologies like Vibration-related methods are used for the primary goal, which is quantification of debonding and delamination of composite layered sections [3, 4]. In response to this limitation, dynamic tests like shock adhesion tests have been developed [37, 15, 6]. The LASAT technique is contactless, involving fast diagnostics based on laser doppler velocimetry and robotizable. It was tuned for evaluating bond strength of plasma sprayed and cold sprayed coatings, as well as electrodeposited coatings and adhesively bonded materials [34, 12]. However, a laser means uses impulsion with a very small characteristic time of about 10^{-9} second [13]. This characteristic time drives the thickness of the structure to be tested. For metallic materials, the thicknesses considered are about of hundreds of microns which corresponds more to a coating than to a structural assembly. Furthermore, the laser pulse creates a strong shock wave at the surface material which may damage the layers, which is not desirable.

The magnetic pulse technology represents an alternative and efficient way to apply a mechanical loading within an electrically conductive layer without creating surface damages, and was already applied as a tensile adhesion test method [19]. This technology allows larger characteristic times of about 10^{-5}s to 10^{-7} seconds. This range of values allows to evaluate the bond strength of laminates of few centimeters thick, which corresponds to structural assemblies. Moreover, the pressures involved are weaker than in the LASAT test : the stress wave propagating in the laminate can not be considered as a shock wave anymore. By the use of these lower pressures, it will be possible to disassemble the laminate, i.e. by interfacial crack, without damaging the layers. Furthermore, the magnetic pulse technology also allows to weld two metallic parts in a dynamic manner [18, 16, 23, 22, 24, 5]. It can produce effects similar to these of explosive welding, with less safety constraints. Finally, such technology can even be used to perform dynamic forming [2, 30, 28, 35] and so to obtain the desired plate shape for a formable material. To sum up, the same technology can be

used to modify the shape, assemble and disassemble laminate structures, which is an interesting invest for manufacturers, both logistically and economically. However for disassembly purpose, a key challenge is to control the tensile stress that can be created at the interface between two layers of a laminate structure, when submitted to a magnetic pulse. Due to the continuous time evolution of the loading, a discontinuous approximation cannot be considered anymore as it was for the design the LASAT test. Rather, the solution method should now account for its continuous time evolution.

The objective of this work is to develop a one dimensional analytical solution in linear elastodynamics giving the expression of the stress created in the laminate structure, when submitted to a magnetic pulse loading. An optimisation problem is then defined, maximising the interfacial tensile stress between the first two layers with respect to a set of unknowns consisting of some geometrical parameters of the laminate, and of material impedances of each layer. The method of characteristics is used to solve the linear elastodynamics problem. For a given unknown vector, and for the sake of simplicity, only the sufficient set of characteristics is considered. Therefore, the solution of the optimisation problem requires to study various configurations of the assembly, each requiring to consider different sets of characteristics in the laminate, in order to explore the domain of feasability. The paper is structured as follows. The linear elastodynamics initial boundary value problem is described in Section 2. Section 3 defines the optimisation problem. Section 4 gives the analytical expressions of the interfacial tensile stress between the first two layers for different configurations of the laminate. Section 5 introduces a two-stage solution procedure to solve the optimisation problem, which is then applied to the configurations studied in Section 4. At last, Sections 6 and 7 study the evolution of the interfacial tensile stress for bi-layers and tri-layers configurations gathering the different aforementioned configurations.

2. Linear elastodynamics initial boundary value problem

Let us consider a laminate structure consisting of a set of stacked homogeneous layers in its thickness along the direction x. The presented situation is assumed being a linear elastodynamic wave propagation, more precisely following the geometrical linearized framework and the isothermal assumption. The laminate is also assumed to be infinite in the in-plane directions y and z, such that a one-dimensional strain state

$$\boldsymbol{\varepsilon} = \varepsilon \mathbf{e}_x \otimes \mathbf{e}_x \tag{1}$$

consistent with the kinematics of a plane wave is achieved, where $\boldsymbol{\varepsilon}$ is the linearized strain tensor. This continuous medium is governed at any time by the following conservation laws

$$\frac{\partial \boldsymbol{\mathcal{U}}}{\partial t} + \frac{\partial \boldsymbol{\mathcal{F}}}{\partial x} = 0, \tag{2}$$

in which the conserved vector variables $\boldsymbol{\mathcal{U}}$ and the fluxes $\boldsymbol{\mathcal{F}}$ are defined as

$$\boldsymbol{\mathcal{U}} = \begin{Bmatrix} \rho v \\ \varepsilon \end{Bmatrix}; \quad \boldsymbol{\mathcal{F}} = \begin{Bmatrix} -\sigma \\ -v \end{Bmatrix}. \tag{3}$$

In vectors (3), ρ, v, ε and $\sigma \equiv \sigma_{xx}$ denote the mass density and the longitudinal components of the material velocity, the linearized strain tensor and of the Cauchy stress tensor respectively. The first equation of System (2) is the conservation of linear momentum, while the second expresses the geometric compatibility between the strain rate and the velocity gradient. Each layer k of the laminate is assumed to follow a linear elastic and isotropic response

$$\boldsymbol{\sigma} = \lambda_k \mathrm{tr}(\boldsymbol{\varepsilon})\mathbf{1} + 2\mu_k \boldsymbol{\varepsilon} \tag{4}$$

where λ_k and μ_k denote Lamé's elastic modulii of the layer k. From Equations (1) and (4), the transverse stress components can be deduced from the longitudinal one and hence do not enter the system of conservation law (2). Following Wang [38], the combination of System (2) and Equation (4) admits the following

rightward (+) and leftward (−) characteristic lines

$$dx = \pm c_k dt \tag{5}$$

in the k^{th} layer, where $c_k = \sqrt{(\lambda_k + 2\mu_k)/\rho_k}$ denotes the associated longitudinal elastic sound speed. Along these characteristic lines, the following compatibility relationships or characteristic equations

$$\begin{cases} dv = \pm c d\varepsilon \\ d\sigma = \pm \rho_k c_k dv \end{cases} \tag{6}$$

are satisfied. One shall notice that the acoustic wave impedance $Z_k = \rho_k c_k$ of layer k is here constant.

The laminate is subjected to a mechanical loading supposed to result from a magnetic pulse applied on its left side. During the electrical discharge, an oscillating current flowing into a coil will generate eddy currents in any electrically conductive medium placed in the vicinity of that coil. Then, repulsive Lorentz forces result from these eddy currents and magnetic induction in these electrically conductive media. It is therefore implicitly assumed in this study that the first layer of the laminate is electrically conductive. It is also known that eddy currents mainly flows within some skin depth of thickness

$$\delta = \sqrt{\frac{2}{\omega \mu_0 \mu_r \kappa}} \tag{7}$$

related to the pulse frequency ω, to the magnetic permeability in vacuum μ_0 and the relative permeability of the material μ_r, and to the electrical conductivity of the medium κ. However for the sake of simplicity, and in order to perform an analytical analysis, such skin depth will be assumed to be far lower than the thickness d_A of the first layer A, namely

$$\frac{\delta}{d_A} << 1 \tag{8}$$

From Equation (8), the spatial distribution of Lorentz forces can be integrated through the skin depth to define an equivalent applied pressure [28, Eq. (15)]. From the expression of the decaying oscillatory discharged current [28, Eq. (3)], an exponentially decreasing square sine signal is obtained for that pressure. However for the sake of simplicity, only the first half semi-period of this signal will be considered in the modelling since it is the most significant in this study. The magnetic pulse applied on the laminate will thus be approximated by the following applied pressure defined at its left side (at $x = 0$)

$$\bar{P}(t) = \begin{cases} P_{\max} \sin^2\left(\dfrac{\pi t}{\tau}\right) & \forall t \in [0, \tau] \\ 0 & \text{otherwise} \end{cases} \tag{9}$$

where the loading time $\tau = \frac{\sqrt{LC}}{\pi}$ can be linked to the inductance L and the capacity C of the electrical circuit, and $P_{\max}$ is the maximum pressure reached, linked to the maximum intensity $I_{\max}$ reached during the discharge.

Next, the right end of the laminate will be considered as a free surface, following the condition :

$$\sigma(x = D, t) = 0 \quad \forall t \geq 0 \tag{10}$$

where D denotes the thickness of the laminate. The laminate is also assumed to be initially at rest in a natural state, yielding

$$\mathbf{u}(x, t = 0) = 0 \quad \forall x \in [0, D], \tag{11}$$

from which zero stresses follows from Equation (4). The combination of System (2), Equation (4), the applied pressure (9), supplemented with the right free boundary (10) and the initial conditions associated with a natural state (11) forms the linear elastodynamics initial boundary value problem. This problem is

hyperbolic and admits a unique solution [21].

3. Definition of the optimisation problems

3.1. Optimisation problem ($\mathcal{P}_0$)

The aim of the optimisation problem ($\mathcal{P}_0$) is to determine the required conditions for disassembling two layers of the laminate whose response is governed by the mechanical initial boundary value problem. Let's consider for simplicity a laminate consisting of three layers denoted A, B and C, of thicknesses d_A, d_B, d_C respectively. Firstly, the analysis will focus on the disassembly of the first two layers A and B of the laminate. Secondly, an approximate failure criterion can be defined on the normal interfacial tensile stress $\sigma(x = d_A, t)$ which is supposed to reach a critical value σ_r to break the interface between the layers A and B. It should be noticed that many critical stress computation method exist [36]. However, in this paper, a simple limit σ_r is considered. It results in an optimisation problem, whose cost function consists of the ratio of this interfacial tensile stress $\sigma(x = d_A, t)$ to the maximum applied pressure $P_{\max}$, which should be maximized at some arbitrary instant $t = T$ for the given magnetic pulse (9). The optimisation is conducted with respect to an array of unknown variables $\mathbf{X}$

$$\mathbf{X} = \{d_A, d_B, d_C, Z_A, Z_B, Z_C, T\} \tag{12}$$

that consists of the thicknesses of the three layers, their acoustic wave impedances and the time T after which the maximum allowable interfacial tensile stress σ_r has been reached. The optimisation problem reads

$$(\mathcal{P}_0): \qquad \max_{\mathbf{X}} \left(\frac{\sigma(x = d_A, t = T; \mathbf{X}, \mathbf{Y})}{P_{\max}} \right) \tag{13}$$

where the interfacial tensile stress $\sigma(x = d_A, t = T; \mathbf{X}, \mathbf{Y})$ depends on the optimisation variables $\mathbf{X}$ but also on known given quantities $\mathbf{Y} = \{\bar{P}(t)\}$ consisting of the applied loading (9) here, through the aforementioned initial boundary value problem. The optimisation problem is conducted under the constraints

$$\mathbf{X} \in (\mathbb{R}^{+*})^7 \tag{14}$$

3.2. Simplifications of the optimisation problem ($\mathcal{P}_0$)

The optimisation problem ($\mathcal{P}_0$) expressed as (13) involves too many unknowns to admit any analytical treatment. Some additional assumptions should thus be added in order to follow such approach. In this way, one key point is to recall that a tensile stress generally appears at the crossing of two unloading waves, see [38] for instance, and that the resulting tensile stress is as intense as the unloading are consequent. Two consequences arise from this idea.

The first one consists in fixing the time T of appearance of the maximum interfacial tensile stress in such a way that it equals the loading time τ plus the time for a rightward elastic wave to propagate in the whole layer A. In other words, the positive characteristic line joining the unloaded state $\sigma(x = 0, t = \tau)$, generating one unloading wave, to the interface between layers A and B, determines the time T at which the maximum interfacial tensile stress should occur. Figure 1 shows the plane (x, t) (the Lagrange diagram), especially the rightward characteristic line plotted in blue joining states 4 and 1 propagates the unloaded state to the interface between the layers A and B. From geometric considerations visible in Figure 1, one gets

$$T = \tau + \frac{d_A}{c_A}, \tag{15}$$

where c_A denotes the longitudinal elastic sound speed in the layer A.

The second one consists in fixing the thickness of layer B in such a way that the maximum applied pressure $P_{\max}$ transmitted to layer B (through the characteristic line joining states 5 and 3, see Figure 1) travels along only one wave round trip in that layer before crossing the previous unloading wave (propagated

along the rightward characteristic line plotted in blue) at time T. Comparing the path of the first unloading wave (blue) and of the second one propagated from P_{max} (green), one gets:

$$\frac{d_A}{c_A} + 2\frac{d_B}{c_B} = \frac{d_A}{c_A} + \frac{\tau}{2}, \tag{16}$$

from which the thickness of layer B is deduced

$$d_B = \frac{\tau c_B}{4} \tag{17}$$

Figure 2 shows the (v, σ) plane associated with the characteristic plane (x, t) shown in Figure 1. It can be observed that the unloaded state 4 is transmitted to states 1 and 2 through characteristics in layers A and B respectively. However, the crossing of two unloading waves associated with characteristics $4-1$ and $2-1$ generates a tensile stress, especially if $Z_B > Z_C$.

However, realistic configurations may not admit such a strict constraint concerning the thickness of layer B (17). One possibility is to relax this condition by allowing an integer number n of wave round trips in layer B before the maximum tensile stress occurs at the interface between the layers A and B at time T. Two configurations then arise. The first one is called B_1 and considers only one wave round trip in the layer B, its thickness is hence given by Equation (17). The second one is called B_n and considers an integer number n of wave round trips performed in the layer B, such that the thickness of layer B is obtained as

$$d_B = \frac{\tau c_B}{4n}, \quad n \in \mathbb{N}^{+*}. \tag{18}$$

For the sake of simplicity, the loading time and the geometry of the laminate are assumed such that there is no wave return at the interface between the layers A and B reflected from the bottom of the layer C, until the maximum interfacial tensile stress occurs at time T. This leads to the condition

$$\frac{d_C}{c_C} > \frac{\tau}{2} \tag{19}$$

Setting the parameters T, d_B and d_C according to Equations (15), (17) (or (18)) and (19) respectively ensures that the interface should break in the fastest possible way with the most intense interfacial tensile stress. The set of Equations (15), (17) (or (18)) and (19) is added to the optimisation problem, now denoted $(\mathcal{P}_1)$, as equality-type or inequality-type constraints.

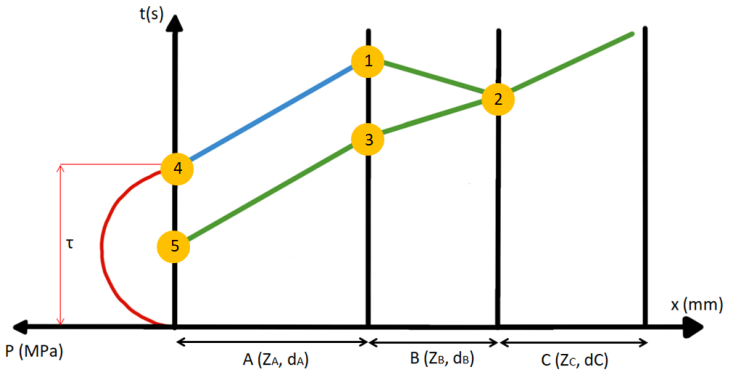

Figure 1: Characteristic plane (x, t) plotted with three layers (A, B, C). Few characteristics lines are plotted from the unloaded state (in blue) and from the maximum loaded one at the left side of the laminate in the three layers (in green). The interface tensile stress reaches its maximum at the crossing of the rightward characteristic joining states 4 and 1, and the leftward characteristic joining states 2 and 1.

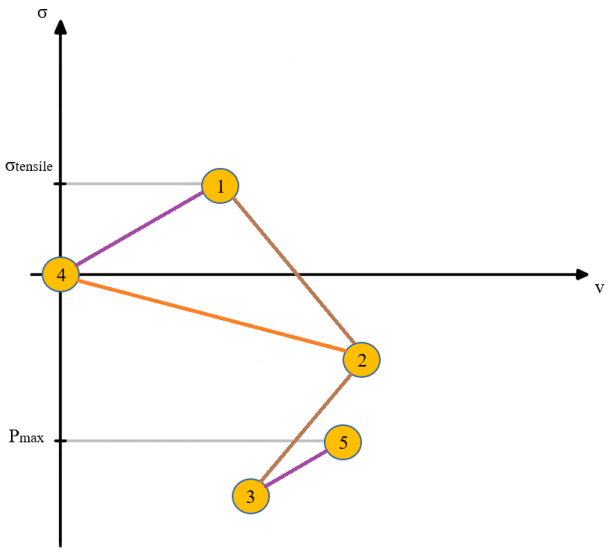

Figure 2: Plane (v, σ) associated with the characteristic plane shown in Figure 1. Lines in purple, brown and orange are associated with the layers A, B and C respectively. The plot is here made in the case $Z_B > Z_A > Z_C$.

4. Elements of solution

4.1. Domain of feasability

The linear elastodynamics initial boundary value problem defined in Section 2 may admit an analytical expression of its solution which is defined in a piecewise manner depending on the chosen instance of the vector $\mathbf{X}$ (12), because its analytical expression is here obtained with the method of characteristics. Hence, the solution of the optimisation problem $(\mathcal{P}_1)$ can be addressed by studying various configurations involving different sets of characteristics in the laminate, associated with different areas of the domain of feasability spanned by the unknown vector $\mathbf{X}$, bounded by the equality-type and inequality-type constraints.

More precisely, the minimal number of considered characteristics which are required to compute the stress between the layers A and B actually depends on the chosen instance of the vector $\mathbf{X}$ (12). Table 2 shows various configurations associated with different numbers of wave round trips within the layers A and B performed during the loading time τ, each denoted A_iB_j, $i \in \{0, 1, n\}$, $j \in \{1, n\}$. The columns of Table 2 illustrate the equality-type constraints (17) and (18) already discussed in Section 3.2, while its rows define three families of configurations according to the number of wave round trips considered in layer A. These can be identified through the following inequalities

$$A_0 : \quad \frac{d_A}{c_A} > \frac{\tau}{2}, \quad A_1 : \quad \frac{\tau}{4} < \frac{d_A}{c_A} < \frac{\tau}{2}, \quad A_n : \quad \frac{d_A}{c_A} < \frac{\tau}{4}. \tag{20}$$

It can be observed that the minimal number of characteristics required to get the sought solution dramatically increases as the ratio $\frac{d_A}{c_A}$ decreases, especially for configurations A_nB_j, $j \in \{1, n\}$.

Remark 1. The configurations A_nB_j, $j \in \{1, n\}$ involve several wave round trips in layer A, which may arise from a very thin layer, a large elastic sound speed or a very long loading time. Notice that these configurations in the case of a thin layer are not consistent with Inequation (8), namely the skin depth within which eddy currents flow can be of the same order of magnitude than thickness of layer A, or are not interesting for the purpose of this study (i.e. dynamic process). Hence, the configurations A_nB_j, $j \in \{1, n\}$ will not be studied in the sequel.

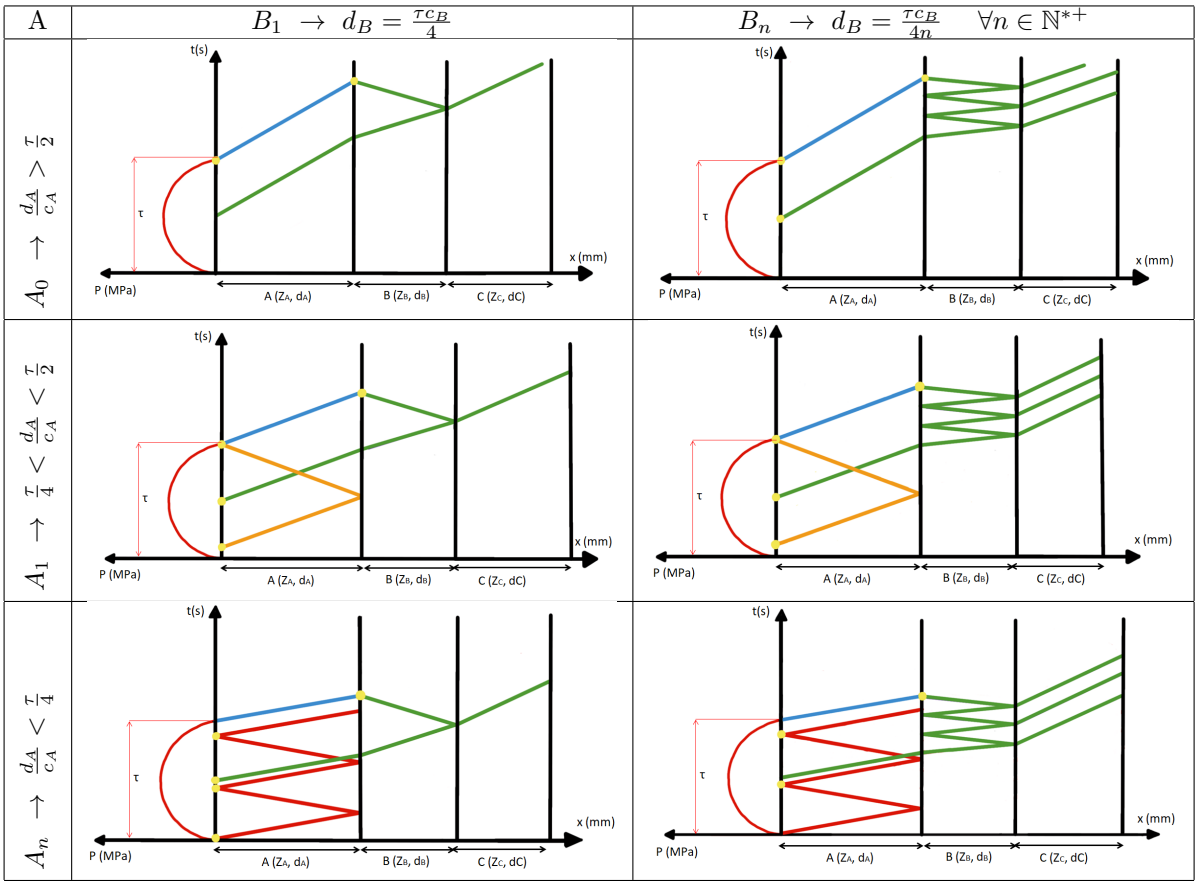

Table 2: Different configurations are depicted with their own sets of characteristic lines. The characteristic line associated with the unloading wave (emanating from $\bar{P}(t = \tau)$) is plotted in blue. These associated with the loading ones, emanating from $\bar{P}\left(t = \frac{\tau}{2}\right) = P_{\max}$ and $\bar{P}(t = 0)$, are plotted in green and red respectively.

Then, analytical expressions are determined for configurations A_0B_1, A_0B_n, A_1B_1 and A_1B_n. Figures showing the characteristic plane (x, t) for each of these configurations always represent the minimum number of characteristic lines necessary to derive the analytical expression of the interfacial stress between the layers A and B, with the same colour-coding than that used in Table 2.

4.2. Configuration A_1B_1

Figure 3 shows the characteristic plane (x, t) associated with the configuration A_1B_1. A set of intermediate points related by characteristic lines are depicted which will allow to determine the value of the tensile stress at point 1, located at the interface between the layers A and B which is expected to break.

From the initial natural condition (11), velocities and stresses can be deduced at the following points of the characteristic plane:

$$\sigma_i = 0 \qquad i = \{2, 7, 8, 10, 11, 12\}, \tag{21}$$

$$v_j = 0 \qquad j = \{7, 8, 10, 11, 12\} \tag{22}$$

The stress at the left side ($x = 0$) of the laminate equals the opposite of the applied pressure (9), especially

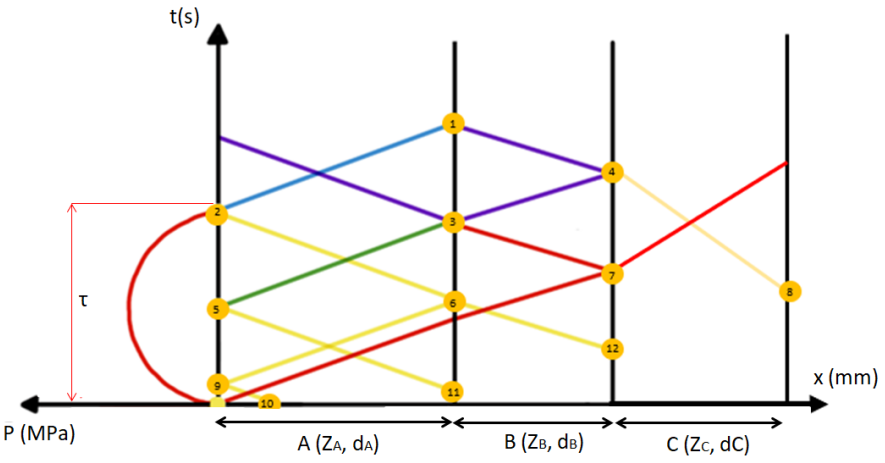

Figure 3: Characteristic plane (x,t) associated with the configuration A_1B_1.

it implies :

$$\sigma_9 = -P_9 \tag{23}$$

$$\sigma_5 = -P_{\max} \tag{24}$$

From these initial and boundary values, the state of other points can successively be deduced using the method of characteristics. Especially the characteristic equation $(6)_2$ integrated along a characteristic line joining states i and j gives :

$$\sigma_i - \sigma_j = \pm Z_k(v_i - v_j) \quad i,j \in \{1,6\}; k \in \{A,B,C\} \tag{25}$$

The expressions of stresses and velocities at each intermediate point are given in Appendix A. The interfacial tensile stress associated with point 1 (see Figure 3) is expressed as :

$$\sigma_1 = 2Z_B \left(\frac{2Z_A P_{\max}(Z_B - Z_C) + P_9(Z_B - Z_A)(Z_C + Z_B)}{(Z_A + Z_B)^2(Z_C + Z_B)} \right), \tag{26}$$

where P_9 is defined as :

$$P_9 = \bar{P}\left(t = \tau - 2\frac{d_A}{c_A}\right), \tag{27}$$

and according to Equation (9), is particularized to

$$P_9 = P_{\max}\sin^2\left(\frac{\pi\left(\tau - 2\frac{d_A}{c_A}\right)}{\tau}\right) = P_{\max}\sin^2\left(\frac{d_A \pi c_B}{2 d_B c_A}\right), \tag{28}$$

where Equation (17) has been used. As a consequence, the interfacial tensile stress computed at point 1 associated with a tri-layer laminate can finally be expressed as

$$\sigma^{Tri}_{A_1B_1} = 2Z_B P_{\max}\left(\frac{2Z_A(Z_B - Z_C) + \sin^2\left(\frac{d_A \pi c_B}{2 d_B c_A}\right)(Z_B - Z_A)(Z_C + Z_B)}{(Z_A + Z_B)^2(Z_C + Z_B)} \right) \tag{29}$$

Remark 2. For a bi-layer laminate, the interface tensile stress is simplified as follows:

$$\sigma^{Bi}_{A_1B_1} = 2Z_B P_{\max}\left(\frac{2Z_A + \sin^2\left(\frac{d_A \pi c_B}{2 d_B c_A}\right)(Z_B - Z_A)}{(Z_A + Z_B)^2}\right) \tag{30}$$

4.3. Configuration A_0B_1

The configuration A_0B_1 is obtained when the time for a wave to travel along the thickness of layer A becomes larger than half of the loading time, and for one wave back and forth in layer B. Figure 4 shows the associated characteristic plane (x,t). This case can be deduced from the previous one (i.e. A_1B_1) setting

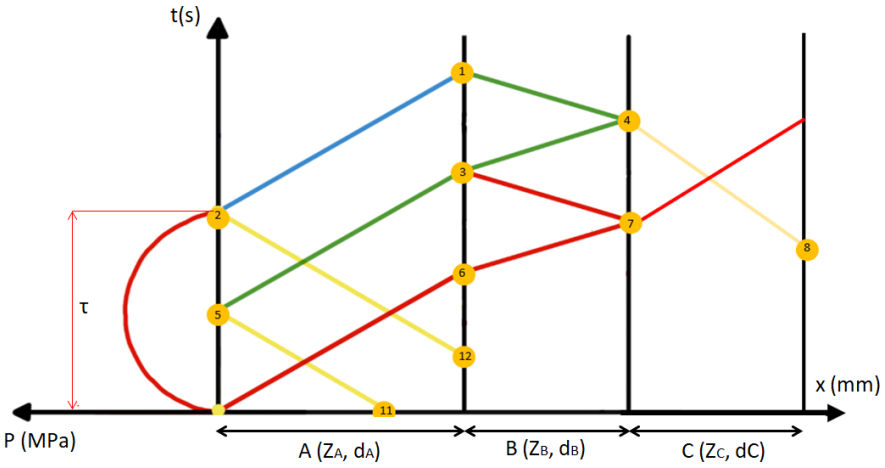

Figure 4: Characteristic plane (x,t) associated with the configuration A_0B_1.

$P_9 = 0$. The velocity and the tensile stress expressed at the interface between the layers A and B can then be deduced from Equations (29) and (28), one gets:

$$v_1 = \frac{4Z_B P_{\max}(Z_B - Z_C)}{(Z_A + Z_B)^2(Z_C + Z_B)}, \tag{31}$$

$$\sigma^{Tri}_{A_0B_1} = \frac{4Z_B Z_A P_{\max}(Z_B - Z_C)}{(Z_A + Z_B)^2(Z_C + Z_B)}. \tag{32}$$

Observe that the sign of the interfacial stress (32) only follows that of $(Z_B - Z_C)$. Especially, a tensile stress is only possible when $Z_B > Z_C$ for configuration A_0B_1, whatever the impedance of layer A.

Remark 3. For a laminate structure consisting of two layers, the interface tensile stress can be simplified as follows :

$$\sigma^{Bi}_{A_0B_1} = \frac{4Z_B Z_A P_{\max}}{(Z_A + Z_B)^2} \tag{33}$$

4.4. Configuration A_0B_n

The B_n configurations are obtained when an integral number n of wave round trips emanating from $P_{\max}$ is considered in the layer B, until the maximum interfacial tensile stress between layers A and B occurs at time T. Figure 5 shows the associated characteristic plane (x,t). From the initial natural condition (11), the velocities and the stresses vanish at some points of the characteristic plane:

$$\begin{cases} \sigma_j = 0 \\ v_j = 0 \end{cases}, \quad j \in \{O_k, P_6, g_6, d_6\}, \quad k \in \{1,2,3,4,5,6,7,8,9,10,11,12,13\}. \tag{34}$$

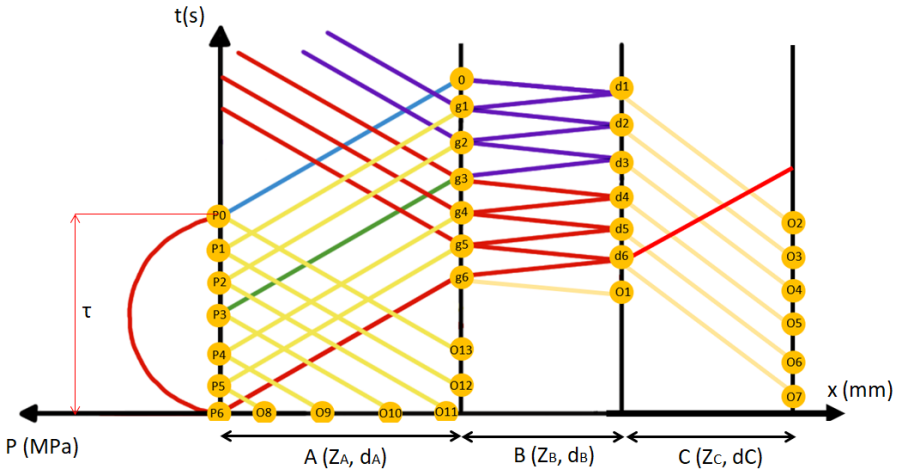

Figure 5: Characteristic plane (x,t) associated with the configuration A_0B_n.

On the left side of the laminate ($x=0$), for an imposed pressure loading pulse, one gets :

$$\begin{cases} \sigma_{P_i} = -P_i \\ v_{P_i} = \frac{P_i}{Z_A} \end{cases}, \quad i \in \{0,1,2,3,4,5,6\}. \tag{35}$$

From these initial values, the states of other points can successively be deduced using the method of characteristic (25). Especially, the states of the points g_i located at the interface between the layers A and B are deduced from the following recurrence formula:

$$\begin{cases} \sigma_{g_i} - \sigma_{d_{i+1}} = -Z_B(v_{g_i} - v_{d_{i+1}}) \\ \sigma_{g_i} - \sigma_{P_i} = Z_A(v_{g_i} - v_{P_i}) \end{cases}, \quad i \in \{0,1,2,3,4,5,6\} \tag{36}$$

The solution of System (36) allows to express states associated with points g_i as a function of these associated with points d_{i+1} and with pressure points P_i

$$\sigma_{g_i} = \frac{Z_A\sigma_{d_{i+1}} + Z_AZ_Bv_{d_{i+1}} - 2Z_BP_i}{Z_A + Z_B}, \tag{37}$$

$$v_{g_i} = \frac{2P_i + \sigma_{d_{i+1}} + Z_Bv_{d_{i+1}}}{Z_A + Z_B}. \tag{38}$$

The states defined at points d_i located at the interface between the layers B and C, are solution of the following recurrence formula:

$$\begin{cases} \sigma_{d_i} - \sigma_{g_i} = Z_B(v_{d_i} - v_{g_i}) \\ -Z_Cv_{d_i} = \sigma_{d_i} \end{cases} \tag{39}$$

whose solution gives expressions

$$v_{d_i} = \frac{Z_Bv_{g_i} - \sigma_{g_i}}{Z_C + Z_B}, \tag{40}$$

$$\sigma_{d_i} = -Z_C\frac{Z_Bv_{g_i} - \sigma_{g_i}}{Z_C + Z_B}. \tag{41}$$

Introducing Equations (40) and (41) into Equations (37) and (38), one gets the recurrence formula:

$$v_{g_i} = \frac{Z_B(Z_B - Z_C)v_{g_{i+1}} + (Z_C - Z_B)\sigma_{g_{i+1}} + 2(Z_C + Z_B)P_i}{(Z_A + Z_B)(Z_C + Z_B)}, \tag{42}$$

$$\sigma_{g_i} = \frac{Z_A Z_B v_{g_{i+1}}(Z_B - Z_C) + Z_A\sigma_{g_{i+1}}(Z_C - Z_B) - 2Z_B(Z_C + Z_B)P_i}{(Z_A + Z_B)(Z_C + Z_B)}. \tag{43}$$

Finally, solving the system consisting of Equations (42) and (43), the stress at points g_i is expressed by recurrence as:

$$\sigma_{g_i} = \frac{(Z_B(Z_B - Z_A - Z_C) + Z_A Z_C)\sigma_{g_{i+1}} - 2Z_B((Z_B + Z_C)P_i - (Z_B - Z_C)P_{i+1})}{(Z_A + Z_B)(Z_B + Z_C)} \tag{44}$$

From equation (44), the interfacial tensile stress for a tri-layer laminate can be expressed for n back and forth in the layer B as follows:

$$\sigma^{Tri}_{A_0B_n} = P_{\max}\sum_{i=1}^{2n-1}\left(\alpha_4^{-i-1}\left(\alpha_1^i\alpha_2 + \alpha_4\alpha_1^{i-1}\alpha_3\right)\sin^2\left(\frac{i\pi}{n}\right)\right) \tag{45}$$

where the following constants have been defined as :

$$\begin{cases} \alpha_1 = Z_B(Z_B - Z_A - Z_C) + Z_A Z_C \\ \alpha_2 = -2Z_B(Z_B + Z_C) \\ \alpha_3 = 2Z_B(Z_B - Z_C) \\ \alpha_4 = (Z_A + Z_B)(Z_B + Z_C) \\ (\alpha_1, \alpha_2, \alpha_3, \alpha_4) \in \mathbb{R}^4 \end{cases} \tag{46}$$

Remark 4. For a laminate structure consisting of two layers, the interface tensile stress simplifies as follows:

$$\sigma^{Bi}_{A_0B_n} = \frac{4P_{\max}Z_B Z_A}{Z_B^2 - Z_A^2}\sum_{i=1}^{2n-1}\left(\left(\frac{Z_B - Z_A}{Z_B + Z_A}\right)^i\sin^2\left(\frac{i\pi}{n}\right)\right) \tag{47}$$

4.5. Configuration A_1B_n

Configurations A_1B_n and A_0B_n are close to each other. The difference lies in that at least one wave round trip can be achieved within layer A during the loading time τ. This is shown in Figure 6 by the characteristic lines plotted in orange. The state at point P_0 is now given by these associated with points g^*, P^* and d^*. The expression of the velocity at point P_0 is changed accordingly. From the initial natural condition (11), Equations (34) still hold, and is supplemented with similar ones at point d^*:

$$\begin{cases} \sigma_{d^*} = 0 \\ v_{d^*} = 0 \end{cases} \tag{48}$$

From the states at points P^*, O_8 and d^*, that at point g^* can be deduced as

$$v_{g^*} = \frac{2P^*}{Z_A + Z_B} \tag{49}$$

$$\sigma_{g^*} = \frac{-2Z_B P^*}{Z_A + Z_B} \tag{50}$$

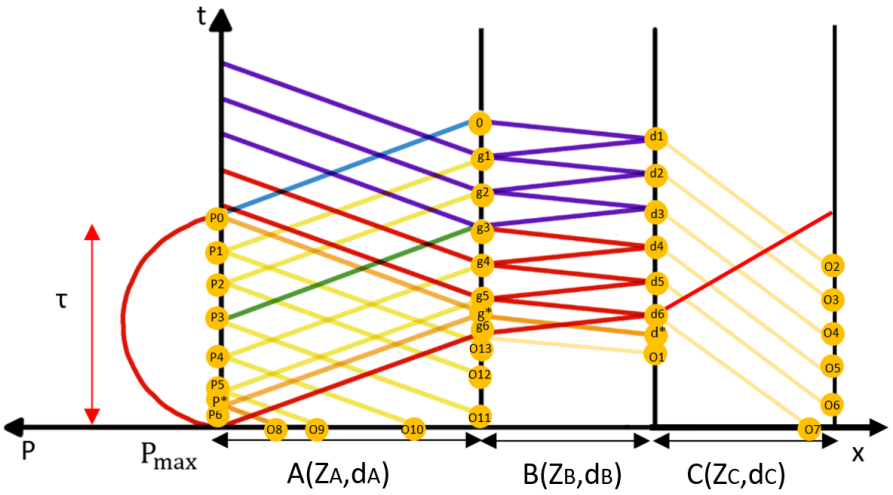

Figure 6: Characteristic plane (x,t) associated with the configuration A_1B_n. The sketch is here made with $n=6$ for illustration purpose, without loss of generality.

from which, the state at location P_0 changes as :

$$v_{P_0} = \frac{-2(Z_B - Z_A)P^*}{Z_A(Z_A + Z_B)} \tag{51}$$

$$\sigma_{P_0} = \frac{-2Z_B P^*}{Z_A + Z_B} \tag{52}$$

From Equations (42) and (43) we can deduce the (σ,v) state at point g_1

$$\sigma_{g_1} = P_{max} \sum_{i=2}^{2n-1} \left(\alpha_4^{-i} \left(\alpha_1^{i-1}\alpha_2 + \alpha_4 \alpha_1^{i-2}\alpha_3 \right) \sin^2\left(\frac{i\pi}{n}\right) \right) + \alpha_2 \alpha_4^{-1} P_1 \tag{53}$$

$$v_{g_1} = P_{max} \sum_{i=2}^{2n-1} \left(\alpha_8^{-i} \left(\alpha_5^{i-1}\alpha_7 + \alpha_5^{i-2}\alpha_8\alpha_6 \right) \sin^2\left(\frac{i\pi}{n}\right) \right) + \alpha_7 \alpha_8^{-1} P_1 \tag{54}$$

with $\alpha_1, \alpha_2, \alpha_3, \alpha_4$ defined by Equations (46) and:

$$\begin{cases} \alpha_5 = (Z_B^2 - Z_A^2)(Z_B^2 - Z_C^2) \\ \alpha_6 = 2((Z_C + Z_B)^2(Z_B + Z_A) \\ \alpha_7 = -2(Z_A + Z_B)(Z_C^2 + Z_B^2) \\ \alpha_8 = (Z_B + Z_A)^2(Z_B + Z_C)^2 \end{cases} \tag{55}$$

Finally, the interfacial tensile stress for the configuration A_1B_n can be deduced as :

$$\sigma^{Tri}_{A_1B_n} = \frac{Z_A P_{max}(Z_B - Z_C)}{(Z_A + Z_B)(Z_B + Z_C)} \sum_{i=2}^{2n-1} \left[\left(\alpha_8^{-i} Z_B (\alpha_5^{i-1}\alpha_7 + \alpha_5^{i-2}\alpha_8\alpha_6) - \right. \right.$$
$$\left. \left. \alpha_4^{-i} \left(\alpha_1^{i-1}\alpha_2 + \alpha_4\alpha_1^{i-2}\alpha_3 \right) \right) \sin^2\left(\frac{i\pi}{n}\right) \right] + \frac{2Z_B(Z_B - Z_A)P_{max}}{(Z_A + Z_B)^2} \sin^2\left(\frac{d_A \pi c_B}{2 d_B c_A}\right) \tag{56}$$

Remark 5. For a laminate structure with two layers, the interfacial tensile stress can be expressed as

follows:

$$\sigma^{Bi}_{A_1B_n} = \frac{2P_{max}Z_B(Z_B - Z_A)}{(Z_A + Z_B)^2} \sin^2\left(\frac{d_A \pi c_B}{2d_B c_A}\right) \tag{57}$$

5. Solution of the optimisation problem

5.1. A two-stage solution procedure

From the unknown vector $\mathbf{X}$ (12), and the set of constraints (15), (17) (or (18)) and (19), two subsets of unknowns can be identified. Observe that if the set of acoustic impedances (Z_A, Z_B, Z_c) of the laminate is fixed, then the thickness of layer B is fixed by Equation (17) (or (18)), that of layer C can be determined by Inequation (19) (and hence can be fixed accordingly) while the time to failure T becomes a function of the thickness of the layer A through Equation (15), which appears to be the sole remaining unknown.

Accordingly, the optimisation problem can be solved following a two-stage procedure. The first one is performed by maximizing the cost function (13) with respect to the sole thickness of the layer A, namely :

$$\mathbf{X} = \{d_A\}, \tag{58}$$

still constrained such that $\mathbf{X} \in (\mathbb{R}^{+*})$, and provided an extended set of given data $\mathbf{Y}$

$$\mathbf{Y} = \{\bar{P}(t), Z_A, Z_B, Z_C\}, \tag{59}$$

including all acoustic impedances of the different layers the laminate consists of. Second, once optimized with respect to d_A at fixed wave impedances, the cost function is maximized with respect to acoustic impedances at given thickness of layer A, such that the following staggered algorithm is considered

$$(d_A, Z_A, Z_B, Z_C) = \arg \max_{(Z_A, Z_B, Z_C)} \max_{d_A} \left(\frac{\sigma(x = d_A, t = T; d_A, Z_A, Z_B, Z_C, \bar{P}(t))}{P_{\max}}\right) \tag{60}$$

5.2. Solution of the optimisation problem for different configurations

In order to solve the optimisation problem (60), one explicit expression of the interfacial tensile stress between layers A and B associated with one of the configurations studied in Section 4 should be selected.

5.2.1. Configurations A_0B_j

From Equations (32), (33), (45) and (47), it can be observed that the configurations A_0B_1 and A_0B_n yield an interfacial tensile stress that only depends on the acoustic impedances either in bi-layered or tri-layered options, but not on the geometry, and especially not on d_A. These configurations do not allow any possibility to increase the interfacial tension via the geometry. Hence only the second stage of the optimisation problem can be conducted, whose solution is trivial and yields

$$\begin{aligned}
&\left(\sigma^{Tri}_{A_0B_1}\right)^{optimal} = P_{\max}, \quad \text{if } Z_A = Z_B,\ Z_C = 0 \\
&\left(\sigma^{Bi}_{A_0B_1}\right)^{optimal} = P_{\max}, \quad \text{if } Z_A = Z_B \\
&\left(\sigma^{Tri}_{A_0B_n}\right)^{optimal} \to 2P_{\max}, \quad \text{if } Z_A \to 0,\ Z_C = 0, n \geq 2 \\
&\left(\sigma^{Bi}_{A_0B_n}\right)^{optimal} \to 2P_{\max}, \quad \text{if } Z_A \to 0, n \geq 2
\end{aligned} \tag{61}$$

Among the A_0B_j configurations, optimal ones are obtained for $Z_C = 0$. Consequently, a third layer should be avoided, a bi-layer laminate is sufficient.

5.2.2. Configurations A_1B_j

Conversely, Equations (29), (30), (56) and (57), obtained for the A_1B_1 and A_1B_n configurations depends on both d_A (i.e. the geometry) and acoustic impedances (Z_A, Z_B, Z_C). Maximising σ_1 in Equations (29), (30), (56) and (57) amounts to maximise $\sin^2\left(\frac{d_A\pi c_B}{2d_B c_A}\right)$ which should equal one, yielding:

$$\frac{d_A\pi c_B}{2d_B c_A} = \frac{\pi}{2} + k\pi \quad \forall k \in \mathbb{N}^{+*} \tag{62}$$

Since the loading only consists of one pulse (see Equation (9)), $k = 0$ can be set. The optimality condition is thus expressed as:

$$\frac{d_A}{d_B} = \frac{c_A}{c_B} \tag{63}$$

Introducing Equation (63) into Equations (29), (30), (56) and (57), the interfacial tensile stress at the interface between the first two layers A and B is given as a function of acoustic impedances by

$$\sigma^{Tri}_{A_1B_1} = 2Z_B P_{\max}\left(\frac{2Z_A(Z_B - Z_C) + (Z_B - Z_A)(Z_C + Z_B)}{(Z_A + Z_B)^2(Z_B + Z_C)}\right) \tag{64}$$

$$\sigma^{Bi}_{A_1B_1} = 2Z_B P_{\max}\left(\frac{2Z_A + (Z_B - Z_A)}{(Z_A + Z_B)^2}\right) \tag{65}$$

$$\sigma^{Tri}_{A_1B_n} = \frac{Z_A P_{max}(Z_B - Z_C)}{(Z_A + Z_B)(Z_B + Z_C)} \sum_{i=2}^{2n-1} \left[\left(\alpha_8^{-i} Z_B(\alpha_5^{i-1}\alpha_7 + \alpha_5^{i-2}\alpha_8\alpha_6)\right.\right. \tag{66}$$

$$\left.\left. - \alpha_4^{-i}\left(\alpha_1^{i-1}\alpha_2 + \alpha_4\alpha_1^{i-2}\alpha_3\right)\right)\sin^2\left(\frac{i\pi}{n}\right)\right] + \frac{2Z_B(Z_B - Z_A)P_{max}}{(Z_A + Z_B)^2}$$

$$\sigma^{Bi}_{A_1B_n} = \frac{2P_{max}Z_B}{(Z_A + Z_B)^2}\left(\frac{Z_A(Z_B - Z_A)}{2(Z_A + Z_B)} - \frac{2Z_B Z_A}{Z_B - Z_A}\sum_{i=1}^{2n-1}\left(\left(\frac{Z_B - Z_A}{Z_B + Z_A}\right)^i \sin^2\left(\frac{i\pi}{n}\right)\right) + (Z_B - Z_A)\right) \tag{67}$$

with $\alpha_1, \alpha_2, \alpha_3, \alpha_4, \alpha_5, \alpha_6, \alpha_7, \alpha_8$ defined in Equations (46) and (55).

The subsequent optimisation of Equations (64), (65), (66), (67) with respect to the wave impedances (Z_A, Z_B, Z_C) gives interesting solutions

$$\left(\sigma^{Tri}_{A_1B_1}\right)^{optimal} \to 2P_{\max}, \quad \text{if } Z_A \to 0,\ Z_B > 0,\ Z_C > 0 \tag{68}$$

$$\left(\sigma^{Bi}_{A_1B_1}\right)^{optimal} \to 2P_{\max}, \quad \text{if } Z_A \to 0,\ Z_B > 0 \tag{69}$$

$$\left(\sigma^{Tri}_{A_1B_n}\right)^{optimal} \to 2P_{\max}, \quad \text{if } Z_A \to 0,\ Z_B > 0,\ Z_C > 0 \tag{70}$$

$$\left(\sigma^{Bi}_{A_1B_n}\right)^{optimal} \to 2P_{\max}, \quad \text{if } Z_A \to 0,\ Z_B > 0 \tag{71}$$

In each of these configurations, twice the maximal pressure applied on the laminate is asymptotically obtained as maximal tensile stress at the interface between layers A and B, at the failure time T. However, these tensile stress should rather be understood as an upper limit since the acoustic impedance Z_A of the first layer A cannot be physically set to zero, and the material of layer A must remain electrically conductive.

But, these results are of great importance. First, it shows that velocity effects can be used at profit to obtain interfacial stress levels which are larger than those achievable in quasi-static. Secondly, since the thickness of the laminate is small with respect to its transverse dimensions by construction, any out-of-plane quasi-static loading would be difficult to set up.

6. Evolution of the interfacial tensile stress spanned by bi-layer configurations

From the optimal results obtained in Section 5.2, the analysis is first focused on a bi-layer laminate structure consisting of the two layers A and B.

6.1. One wave round trip in the layer B

Figure 7 shows a semi-analytical plot of the evolution of the ratio of the interfacial tensile stress to the maximum applied pressure $P_{\max}$ as a function of the ratio $\frac{d_A}{c_A}$, namely the time for a pressure wave to travel through the thickness of the layer A. Indeed, following Inequations (20), this parameter allows to span the different configurations studied in this work. Accordingly, the areas observed in Figure 7 appearing in green, yellow and red correspond to the configurations A_nB_1, A_1B_1 and A_0B_1 respectively. One shall notice that all are given for a single wave round trip in layer B before the interfacial failure occurs.

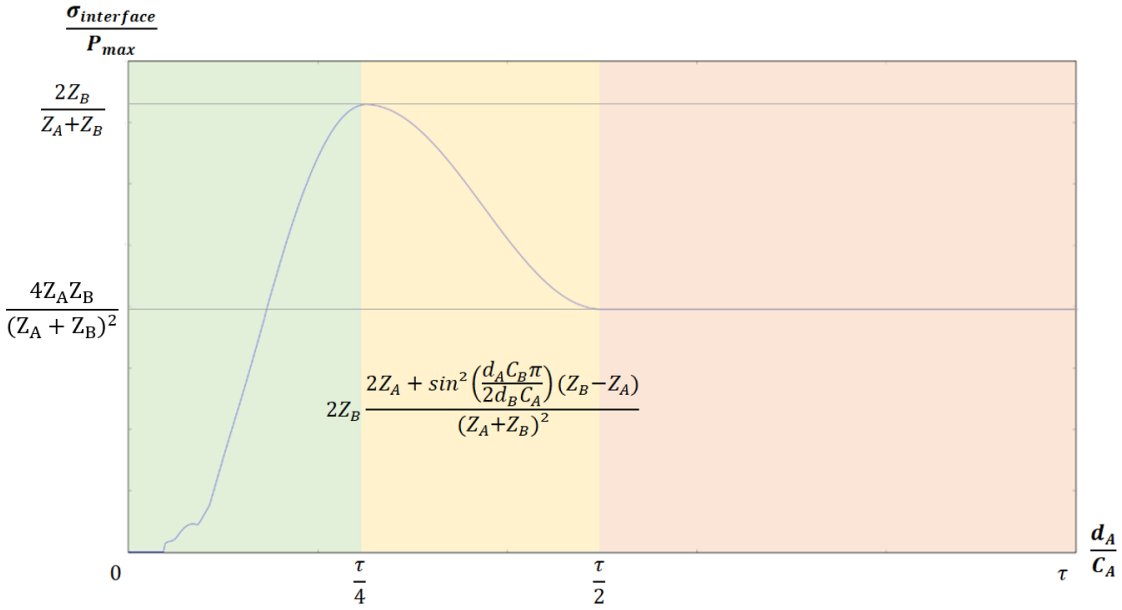

Figure 7: Semi-analytical plot of the interface tensile stress as a function of $\frac{d_A}{c_A}$. Green, yellow and red areas are respectively associated with the configurations A_nB_1, A_1B_1 and A_0B_1. The plot has been performed with the couple aluminium-steel for the layers A and B, whose material parameters are gathered in Table 3.

The first area (appearing in green in Figure 7) is associated with the A_nB_1 configuration and was not studied analytically in Section 4 as already explained in Remark 1. The plot was performed using one-dimensional numerical simulations carried out with a finite volume-type discretization, and more precisely with the Lax-Wendroff scheme [20, 21, 17] which is second order accurate. This plot shows that the interfacial tensile stress increases from zero to the optimal value $2\frac{Z_B}{Z_A+Z_B}$ reached at $\frac{d_A}{c_A} = \frac{\tau}{4}$, the small step at the beginning of the rising edge are numerical effects. The subarea associated with its lowest values is not interesting, and may in addition violate the assumption (8), while its highest values appear much more interesting although the associated subarea was not quantified analytically.

The second area (appearing in yellow in Figure 7) is associated with the A_1B_1 configuration, whose interfacial tensile stress (29) is simplified when considering $Z_C = 0$ as :

$$\sigma_1 = 2Z_B P_{\max}\left(\frac{2Z_A + \sin^2\left(\frac{d_A\pi c_B}{2d_B c_A}\right)(Z_B - Z_A)}{(Z_A+Z_B)^2}\right). \tag{72}$$

The stress ratio ranges in this area from its highest value $2\frac{Z_B}{Z_A+Z_B}$ reached at $\frac{d_A}{c_A} = \frac{\tau}{4}$ (i.e. combining the optimality condition (63) to the equality-type constraint (17)), to its lowest value $\frac{4Z_BZ_A}{(Z_A+Z_B)^2}$ associated with a plateau reached at $\frac{d_A}{c_A} = \frac{\tau}{2}$. Notice that if $\frac{Z_A}{Z_B} \to 0$, these highest and lowest values tend to 2 and zero respectively, while they both tend to unity if $\frac{Z_A}{Z_B} \to 1$. The latter case thus appears less interesting than the former one for disassembling the laminate.

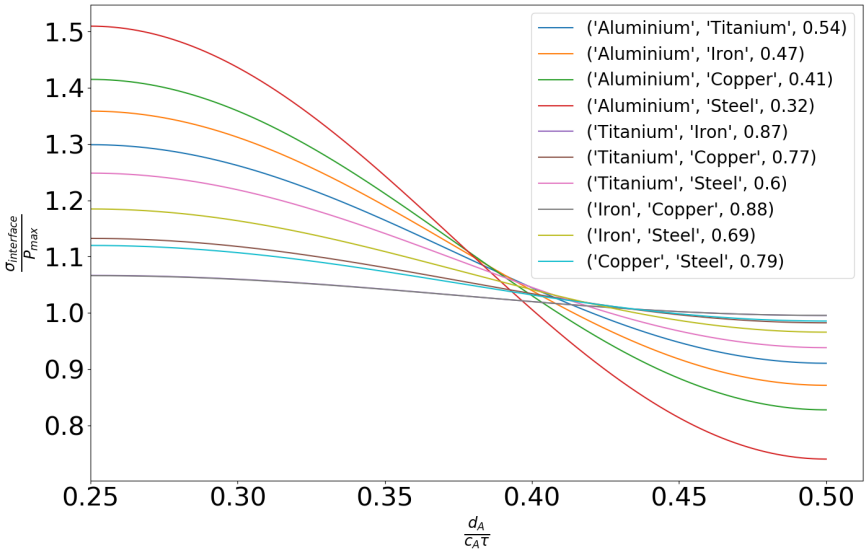

Figure 8: Evolution of the ratio of the interface tensile stress to the maximum applied pressure in the A_1B_1 configuration, plotted for different couples of materials for layers A and B. The legend is of the form : ('Material of the layer A', 'Material of the layer B', $\frac{Z_A}{Z_B}$).

Material	Aluminium	Titanium	Iron	Copper	Steel	CFRP
c (m.s^{-1})	5.38×10^3	5.99×10^3	3.93×10^3	3.94×10^3	5.74×10^3	3.00×10^3
Z (Pa.m.s^{-1})	1.45×10^7	2.69×10^7	3.08×10^7	3.51×10^7	4.47×10^7	0.49×10^7

Table 3: Materials parameters. CFRP stands for Carbon Fiber Reinforced Polymer, data taken from [14]

.

Figure 8 shows some instance of evolutions of this stress ratio for various couples of materials listed in Table 3. A turning point makes a separation between values of the stress ratio increasing up to its maximum value, and these tending to the plateau value observed in Figure 7, whose contrast becomes maximal as $\frac{Z_A}{Z_B} \to 0$, and minimal as $\frac{Z_A}{Z_B} \to 1$. This point is associated with the change of sign of the second derivative of the interface tensile stress (72). Considering Equation (17), its sign is given by that of $\cos\left(\frac{4\pi d_A}{\tau c_A}\right)$ which changes from negative to positive for

$$\frac{d_A}{c_A} = \frac{3}{8}\tau. \tag{73}$$

Hence, for a given instance of couple of materials and if this configuration is targeted, we shall always try to achieve a ratio $\frac{d_A}{c_A}$ lying between the interval $\frac{d_A}{c_A} \in \left[\frac{\tau}{4}, \frac{3}{8}\tau\right]$ bounded by Equations (63) and (73).

The third area (appearing in red in Figure 7) is associated with the A_0B_1 configuration, within which the stress ratio is given by $\frac{4Z_BZ_AP_{max}}{(Z_A+Z_B)^2}$ and does not depends on $\frac{d_A}{c_A}$. As already said, it varies between

zero and $P_{\max}$ for $\frac{Z_A}{Z_B} \to 0$ and $\frac{Z_A}{Z_B} \to 1$ respectively. The latter case corresponds to similar materials in the two layers. Such configuration may be sufficient to disassemble the laminate without damaging it if the bond strength between the two layers is weak. More generally, such magnetic pulse loading applied on a homogeneous structure can be used in magnetic pulse peening [29] for instance, but whose purpose is different from disassembly.

Figure 9 shows the evolution of the stress ratio $\frac{\sigma_{\text{interface}}}{P_{\max}}$ for the two configurations A_0B_1 and A_1B_1 as a function of the ratio of acoustic impedances $\frac{Z_A}{Z_B} \in [0, 1]$. Although these two solutions are equal for $\frac{Z_A}{Z_B} = 1$, they diverge when $\frac{Z_A}{Z_B}$ decreases to zero, where the stress ratio goes to zero for configuration A_0B_1, and tends to 2 for configuration A_1B_1.

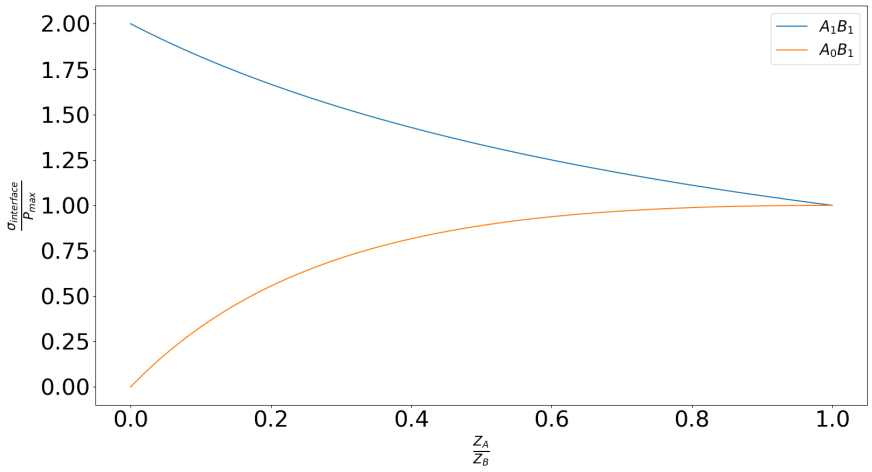

Figure 9: Evolution of the stress ratio as a function of the ratio of acoustidc impedances $\frac{Z_A}{Z_B}$ for the configuration A_0B_1 and A_1B_1.

6.2. Several wave round trips in layer B

As mentioned in Sections 3.2, 4.4 and 4.5, more possibilities in the design of the disassembly process can be obtained by allowing an integer number n of wave round trips in layer B before the time to failure T.

Figures 10 and 11 show, respectively for configurations A_0B_n and A_1B_n, the evolution of the stress ratio as a function of $\frac{Z_A}{Z_B}$ for two or more round trips n of the wave front in layer B before the time T. As it can be seen in Figure 10, the number of round trips n has a huge influence on the interfacial tensile stress. Moreover, for a number of round trips greater or equal than four, there exits an impedance ratio $\frac{Z_A}{Z_B}$ for which the interfacial stress ratio $\frac{\sigma_{\text{interface}}}{P_{\max}}$ admits a maximum (close to 0.9). Hence, the smaller the ratio $\frac{Z_A}{Z_B}$, the more round trips for increasing the interfacial tensile stress. But none of these configurations gives a higher interfacial tensile stress than that obtained with the configuration A_0B_1. Figure 11 shows that, for the A_1B_n configurations, the number of round trips n doesn't have any influence on the interfacial tensile stress when there are only two layers as it can be seen in Equation (57), all plots are superposed. It can also be seen that the maximum interfacial tensile stress is reached for $\frac{Z_A}{Z_B} \to 0$.

7. Evolution of the interfacial tensile stress spanned by the tri-layer configurations

In this section, the analysis is focused on a tri-layered laminate. The stress ratio $\frac{\sigma_{\text{interface}}}{P_{\max}}$ now depends on the ratios $\frac{Z_A}{Z_B}$ and $\frac{Z_C}{Z_B}$.

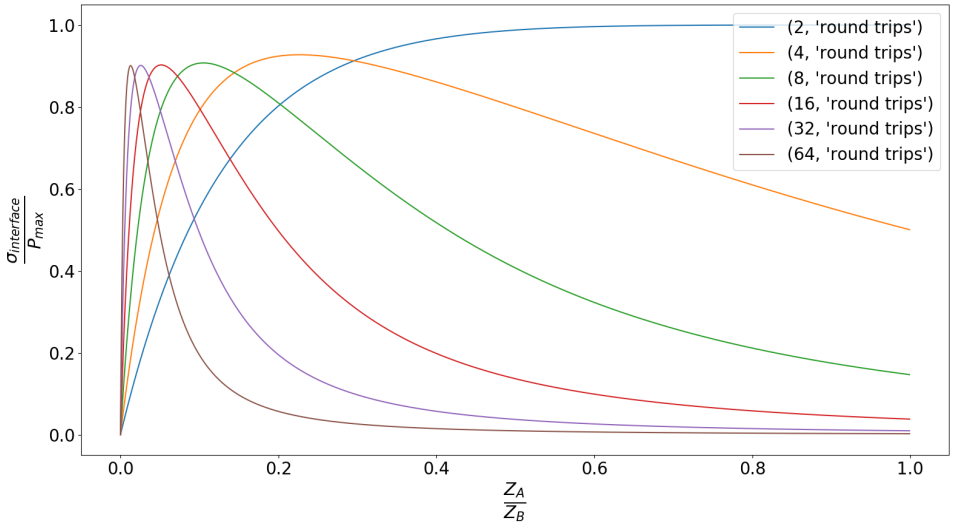

Figure 10: Evolution of the stress ratio for the A_0B_n configuration as a function of the ratio of acoustic impedances $\frac{Z_A}{Z_B}$.

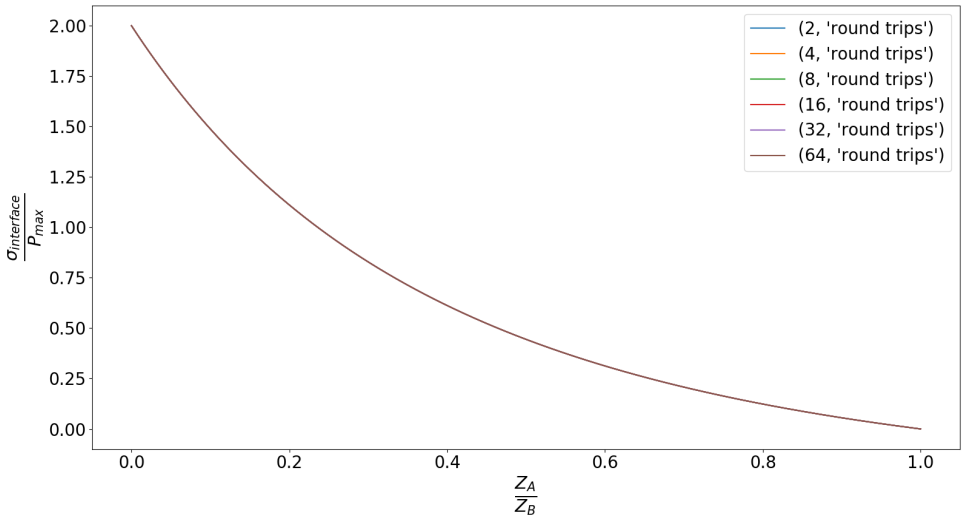

Figure 11: Evolution of the stress ratio for the A_1B_n configuration as a function of the ratio of acoustic impedances $\frac{Z_A}{Z_B}$. Equation (57) does not depend on n. All curves are superposed.

7.1. One wave round trip in the layer B

7.1.1. Evolution of the interface tensile stress for the A_0B_1 configuration

Figure 12 shows the evolution of the stress ratio as a function of these impedance ratios for an A_0B_1 configuration. It can be seen that the impedance of the third layer C has a huge influence on the stress ratio. It highlights the fact that a bi-layer laminate with $\frac{Z_A}{Z_B} \to 1$ should be preferred to this configuration.

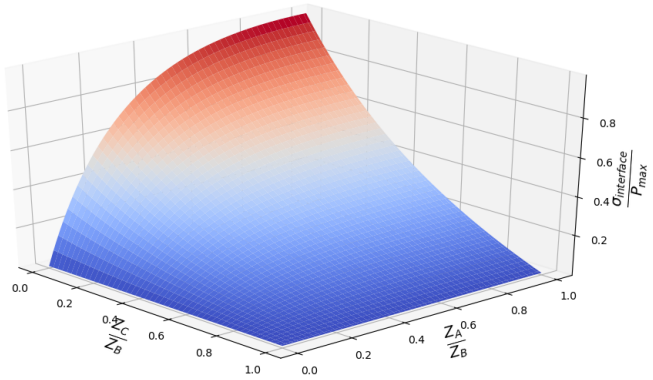

Figure 12: Evolution of the stress ratio for the A_0B_1 configuration as a function of the ratios of wave impedance $\frac{Z_A}{Z_B}$ and $\frac{Z_C}{Z_B}$.

7.1.2. Evolution of the interfacial tensile stress for A_1B_1 configuration

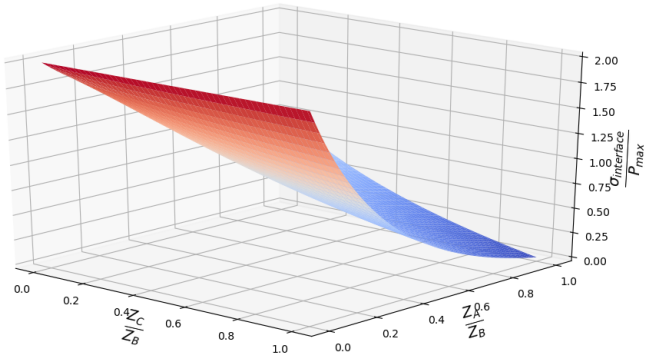

Figure 13: Evolution of the stress ratio for the A_1B_1 configuration as a function of the ratios of wave impedances $\frac{Z_A}{Z_B}$ and $\frac{Z_C}{Z_B}$.

Figure 13 shows the evolution of the stress ratio for the A_1B_1 configuration. The impedance value of the third layer has now a weak influence on the interfacial tensile stress level. The smaller the ratio $\frac{Z_A}{Z_B}$, the weaker this influence. It can be seen that a configuration where $\frac{Z_A}{Z_B} \to 0$ should be preferred regardless the impedance value of the third layer. For this configuration Equation (63) has been considered.

7.2. Several wave round trips in the layer B

7.2.1. Evolution of the interfacial tensile stress for A_0B_n configurations

Figures 14a, 14b, 14c and 14d show the evolution of the interface tensile stress as a function of ratios $\frac{Z_A}{Z_B}$ and $\frac{Z_C}{Z_B}$ for configurations A_0B_2, A_0B_4, A_0B_8 and A_0B_{16} respectively. These four configurations have been chosen to illustrate the evolution of the behaviour of A_0B_n ones. It can be seen that the third layer have a huge negative influence on the interfacial tensile stress. Moreover, the more round trip, the smaller the impedance ratio $\frac{Z_A}{Z_B}$, as already shown in Figure 10. It can be deduced that the optimal configuration of the A_0 configurations is the A_0B_1 with $Z_C = 0$.

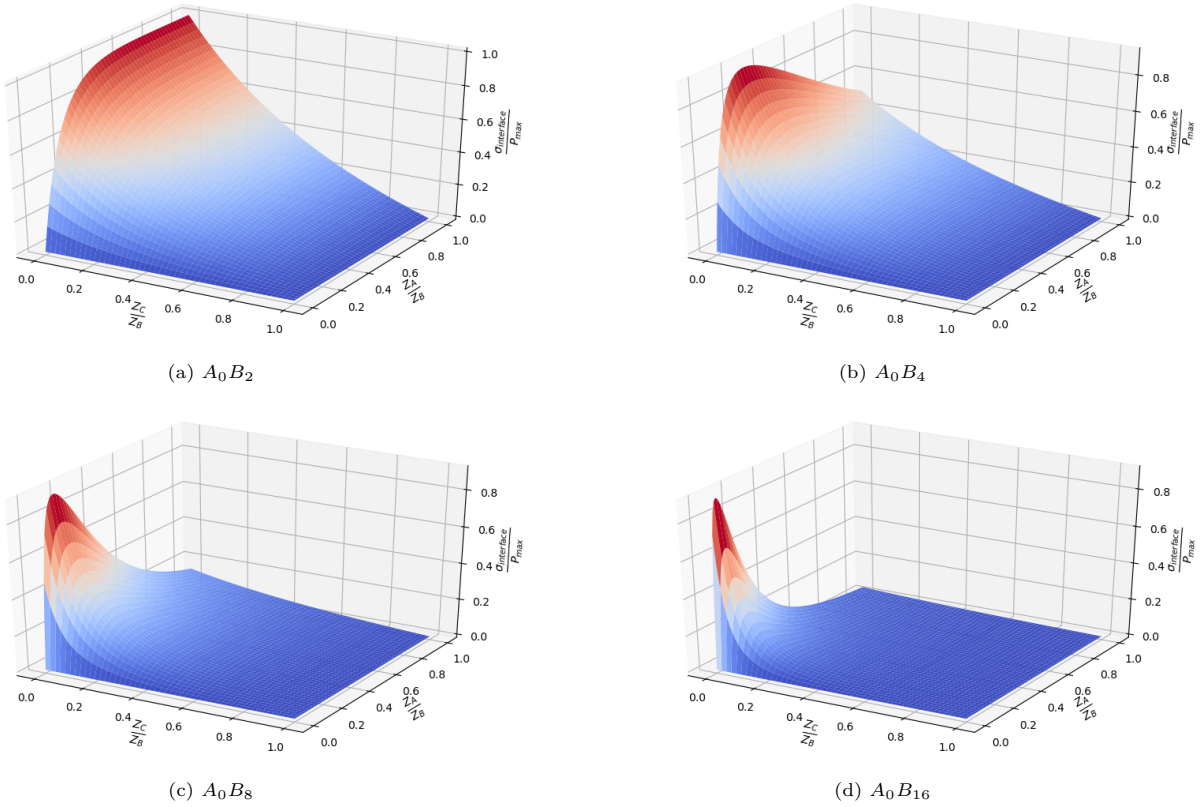

(a) A_0B_2 (b) A_0B_4

(c) A_0B_8 (d) A_0B_{16}

Figure 14: Evolutions of the interfacial tensile stress for A_0B_n configurations, as a function of acoustic impedance ratios.

7.2.2. Evolution of the interfacial tensile stress for A_1B_n configurations

Figures 15a, 15b, 15c and 15d show the evolution of the interface tensile stress as a function of ratios $\frac{Z_A}{Z_B}$ and $\frac{Z_C}{Z_B}$ for configurations A_1B_2, A_1B_4, A_1B_8 and A_1B_{16}. These four configurations have been chosen to illustrate the evolution of the behaviour for A_1B_n ones. For these configurations, it can be seen that the impedance of the layer C and the number of wave round trips n in the layer B before the appearance of the failure do not have a strong influence on the stress ratio. So, it can be concluded that for A_1B_n configurations the presence of a third layer and the number of round trips do not matter. The only constraint to enforce is $\frac{Z_A}{Z_B} \to 0$.

8. Conclusion

The aim of this study was to evaluate by analytical considerations whether or not it would be possible to use the magnetic pulse technology for disassembling laminate structures. This work focused on the study of a one-dimensional model in linear elastodynamics of a laminate consisting of three stacked elastic, homogeneous and isotropic layers, infinite in transverse directions. The method of characteristics was used to solve this model in various configurations. The solution of an optimisation problem, whose purpose was to maximise the interfacial tensile stress between the first two layers with respect to layer thicknesses and acoustic impedances, allowed to draw a set of conclusions. First, the layer B needs to be the one with the highest impedance. Second, adding a third layer C does not appear necessary to increase the interfacial tensile stress. Rather, it contributes to its decreasing. Third, several configurations have been identified as being potentially able to achieve a debonding between the first two layers. Next, it was shown that the interfacial stress follows a three-subarea profile as function of the parameter $\frac{d_A}{c_A}$. In its second subarea,

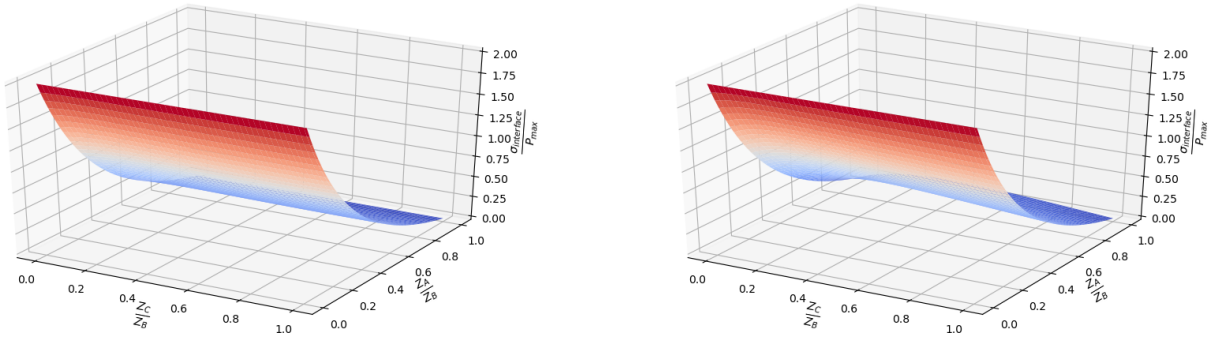

(a) A_1B_2 (b) A_1B_4

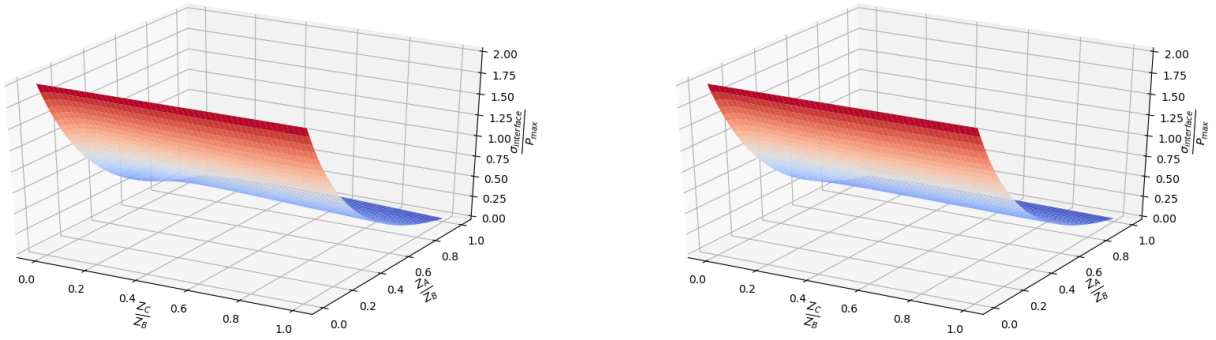

(c) A_1B_4 (d) A_1B_{16}

Figure 15: Evolutions of the interfacial tensile stress for A_1B_n configurations, as a function of acoustic impedance ratios.

given for $\frac{\tau}{4} \leq \frac{d_A}{c_A} \leq \frac{\tau}{2}$, optimised configurations were found for which the interfacial tensile stress has an asymptotic limit of $2P_{\max}$ if $\frac{Z_A}{Z_B} \rightarrow 0$. These promising results point out the interest for developing an experimental device able to disassemble multi-material assemblies which are thicker than a centimeter, as they can be found in light weight armouring plates, including a composite material on ceramic coating or metallic plate for instance. This will be the object of the next step.

Acknowledgments

Benoit Lagain is funded on the one hand by Agence de l'Innovation de Défense (AID) grant reference number 2021 65 0044, and on the other hand by Ecole Centrale de Nantes.

Conflict of interests

The authors declare they have no conflict of interets.

Appendix A. Computation of states at intermediate points for the configuration A_1B_1

Point 9 (from 10) :

$$v_9 = \frac{P_9}{Z_A} \tag{A.1}$$

Point 6 (from 9 and 12):

$$v_6 = \frac{2P_9}{Z_A + Z_B} \tag{A.2}$$

$$\sigma_6 = \frac{-2Z_B P_9}{Z_A + Z_B} \tag{A.3}$$

Point 5 (from 11):

$$v_5 = \frac{P_{max}}{Z_A} \tag{A.4}$$

Point 3 (from 5 and 7):

$$v_3 = \frac{2P_{max}}{Z_A + Z_B} \tag{A.5}$$

$$\sigma_3 = \frac{-2Z_B P_{max}}{Z_A + Z_B} \tag{A.6}$$

Point 4 (from 8 and 3)

$$v_4 = \frac{4Z_B P_{max}}{(Z_A + Z_B)(Z_C + Z_B)} \tag{A.7}$$

$$\sigma_4 = \frac{-4Z_B Z_C P_{max}}{(Z_A + Z_B)(Z_C + Z_B)} \tag{A.8}$$

Point 2 (from 6)

$$v_2 = \frac{2P_9(Z_A - Z_B)}{Z_A(Z_A + Z_B)} \tag{A.9}$$

Point 1 (from 2 and 4) :

$$v_1 = \frac{4Z_B P_{max}(Z_B - Z_C) + 2P_9(Z_A - Z_B)(Z_C + Z_B)}{(Z_A + Z_B)^2(Z_C + Z_B)} \tag{A.10}$$

$$\sigma_1 = 2Z_B \left(\frac{2Z_A P_{max}(Z_B - Z_C) - P_9(Z_A - Z_B)(Z_C + Z_B)}{(Z_A + Z_B)^2(Z_C + Z_B)} \right) \tag{A.11}$$

References

[1] Teklit Gebregiorgis Ambaye, Mentore Vaccari, Shiv Prasad, Eric D van Hullebusch, and Sami Rtimi. Preparation and applications of chitosan and cellulose composite materials. *Journal of Environmental Management*, 301:113850, 2022.

[2] F Bay and J Alves. A computational model for magnetic pulse forming processes–application to a test case and sensitivity to dynamic material behaviour. In *8th International Conference on High Speed Forming*, 2018.

[3] Chiara Bedon. Diagnostic analysis and dynamic identification of a glass suspension footbridge via on-site vibration experiments and fe numerical modelling. *Composite Structures*, 216:366–378, 2019.

[4] Chiara Bedon. Issues on the vibration analysis of in-service laminated glass structures: analytical, experimental and numerical investigations on delaminated beams. *Applied Sciences*, 9(18):3928, 2019.

[5] A Ben-Artzy, A Stern, N Frage, V Shribman, and O Sadot. Wave formation mechanism in magnetic pulse welding. *International Journal of Impact Engineering*, 37(4):397–404, 2010.

[6] C Bolis, Laurent Berthe, M Boustie, M Arrigoni, Sophie Barradas, and Michel Jeandin. Physical approach to adhesion testing using laser-driven shock waves. *Journal of Physics D: Applied Physics*, 64(10):108, 2014.

[7] Muriel Braccini and Michel Dupeux. *Mechanics of solid interfaces*. ISTE Wiley, 2012.

[8] R Ciardiello, L Greco, M Miranda, F Di Sciullo, and L Goglio. Experimental investigation on adhesively bonded u-shaped metallic joints using the arcan test. *Journal of Advanced Joining Processes*, 1:100010, 2020.

[9] Trevor William Clyne and Derek Hull. *An introduction to composite materials*. Cambridge university press, 2019.

[10] Romain Créac'Hcadec, Laurent Sohier, Christophe Cellard, and Bernard Gineste. A stress concentration-free bonded arcan tensile compression shear test specimen for the evaluation of adhesive mechanical response. *International Journal of Adhesion and Adhesives*, 61:81–92, 2015.

[11] Thibaut de Resseguier, Emilien Lescoute, Guillaume Morard, and Francois Guyot. Dynamic fragmentation as a possible diagnostic for high pressure melting in laser shock-loaded iron. In *AIP Conference Proceedings*, volume 1195, pages 1007–1010. American Institute of Physics, 2009.
[12] R Ecault, M Boustie, L Berthe, F Touchard, L Chocinski-Arnault, H Voillaume, and B Campagne. Development of the laser shock wave adhesion test on bonded cfrp composite. *International Journal of Structural Integrity*, 2014.
[13] E Gay, L Berthe, M Boustie, M Arrigoni, A Johnston, R Cole, J Barroeta, and E Buzaud. Experimental and numerical investigation of composite behaviour at high strain rate. In *Proceeding of the 18th DYMAT Technical Meeting, Strasbourg, France*, 2010.
[14] E. Gay, L. Berthe, M. Boustie, M. Arrigoni, and M. Trombini. Study of the response of cfrp composite laminates to a laser-induced shock. *Composites Part B: Engineering*, 64:108–115, 2014.
[15] V Gupta, AS Argon, DM Parks, and JA Cornie. Measurement of interface strength by a laser spallation technique. *Journal of the Mechanics and Physics of Solids*, 40(1):141–180, 1992.
[16] Marlon Hahn, Christian Weddeling, Joern Lueg-Althoff, and A Erman Tekkaya. Analytical approach for magnetic pulse welding of sheet connections. *Journal of Materials Processing Technology*, 230:131–142, 2016.
[17] T. Heuzé. Lax-Wendroff and TVD finite volume methods for unidimensional thermomechanical numerical simulations of impacts on elastic–plastic solids. *Journal of Computational Physics*, 346:369–388, 2017.
[18] Angshuman Kapil and Abhay Sharma. Magnetic pulse welding: an efficient and environmentally friendly multi-material joining technique. *Journal of Cleaner Production*, 100:35–58, 2015.
[19] Sol Krongelb. *Electromagnetic tensile adhesion test method*. ASTM International, 1978.
[20] P. Lax and B. Wendroff. Systems of conservation laws. *Communications on Pure and Applied mathematics*, 13(2):217–237, 1960.
[21] Randall J LeVeque et al. *Finite volume methods for hyperbolic problems*, volume 31. Cambridge university press, 2002.
[22] Jia-Ning Li, Ji-Shuai Li, Wen-Jun Qi, and Ke-Gao Liu. Characterization and mechanical properties of thick tc4 titanium alloy sheets welded joint by vacuum ebw. *Vacuum*, 168:108812, 2019.
[23] Jishuai Li, Rija Nirina Raoelison, Thaneshan Sapanathan, Guillaume Racineux, and Mohamed Rachik. Assessing the influence of fieldshaper material on magnetic pulse welded interface of al/cu joints. *Procedia Manufacturing*, 29:337–344, 2019.
[24] JS Li, RN Raoelison, Thaneshan Sapanathan, YL Hou, and M Rachik. Interface evolution during magnetic pulse welding under extremely high strain rate collision: mechanisms, thermomechanical kinetics and consequences. *Acta Materialia*, 195:404–415, 2020.
[25] Marc A Meyers. *Dynamic behavior of materials*. John wiley & sons, 1994.
[26] Kash L Mittal. *Adhesion measurement of films and coatings*. CRC Press, 2014.
[27] David Ernest Packham. *Handbook of adhesion*. John Wiley & Sons, 2006.
[28] Verena Psyk, D Risch, Brad L Kinsey, A Erman Tekkaya, and M Kleiner. Electromagnetic forming—a review. *Journal of Materials Processing Technology*, 211(5):787–829, 2011.
[29] Emmanuel Sonde, Thibaut Chaise, Daniel Nelias, and Vincent Robin. Numerical simulation of electromagnetic surface treatment. *Journal of Applied Physics*, 123(4):045901, 2018.
[30] Cheikh Tidiane Sow, Grégoire Bazin, Thomas Heuzé, and Guillaume Racineux. Electromagnetic flanging: from elementary geometries to aeronautical components. *International Journal of Material Forming*, 13(3):423–443, 2020.
[31] Georgios Stamoulis, Nicolas Carrère, J-Y Cognard, Peter Davies, and Claudiu Badulescu. Investigating the fracture behavior of adhesively bonded metallic joints using the arcan fixture. *International Journal of Adhesion and Adhesives*, 66:147–159, 2016.
[32] M. L. Su, J. N. Li, K. G. Liu, W. J. Qi, F. Weng, Y. B. Zhang, and J. S. Li. Mechanical property and characterization of ta1 titanium alloy sheets welded by vacuum electron beam welding. *Vacuum*, 159:315–318, 2019.
[33] Mo-Lin Su, Ji-Shuai Li, Wen-Jun Qi, and Jia-Ning Li. Impact performance and microstructures of thick ta1 titanium alloy sheets welded by vacuum electron beam. *Physica Scripta*, 94(11):115703, 2019.
[34] Gilles Tahan, Michel Arrigoni, Pierre Bidaud, Laurent Videau, and David Thévenet. Evolution of failure pattern by laser induced shockwave within an adhesive bond. *Optics & Laser Technology*, 129:106224, 2020.
[35] Jesse D Thomas, Nicolas Triantafyllidis, A Vivek, Glenn S Daehn, and John R Bradley. Comparison of fully coupled modeling and experiments for electromagnetic forming processes in finitely strained solids. *International journal of fracture*, 163(1):67–83, 2010.
[36] Konstantinos Tserpes, Alberto Barroso-Caro, Paolo Andrea Carraro, Vinicius Carrillo Beber, Ioannis Floros, Wojciech Gamon, Marcin Kozlowski, Fabio Santandrea, Moslem Shahverdi, Davor Skejić, et al. A review on failure theories and simulation models for adhesive joints. *The Journal of Adhesion*, 98(12):1855–1915, 2022.
[37] JL Vossen. *Measurements of film-substrate bond strength by laser spallation*. ASTM International, 1978.
[38] Lili Wang. *Foundations of stress waves*. Elsevier, 2011.